

A new semi-coherent targeted search for continuous gravitational waves from pulsars in binary systems

L. Mirasola,^{2,4, a} P. Leaci,^{1,3} P. Astone,³ L. D’Onofrio,³ S. Dall’Osso,^{1,3} A. De Falco,^{2,4}
M. Lai,⁵ S. Mastrogiovanni,³ C. Palomba,³ A. Riggio,^{2,4,6} and A. Sanna^{2,4}

¹*Physics Department, Università di Roma “Sapienza”, P.le A. Moro, 2, I-00185 Roma, Italy*

²*Physics Department, Università degli Studi di Cagliari, Cagliari 09042, Italy*

³*INFN, Sezione di Roma, P.le A. Moro, 2, I-00185 Roma, Italy*

⁴*INFN, Sezione di Cagliari, Cagliari 09042, Italy*

⁵*Department of Physics and Astronomy, University of California, Riverside, CA 92521, USA*

⁶*INAF/IASF Palermo, via Ugo La Malfa 153, I-90146 - Palermo, Italy*

We present a novel semi-coherent targeted search method for continuous gravitational waves (CW) emitted by pulsars in binary systems. The method is based on a custom optimization of the coherence time according to the orbital parameters and their uncertainties, as provided by electromagnetic observations. While rotating pulsars are expected to produce quasi-monochromatic CWs in their reference frame, their orbital motion introduces an additional modulation in the observer frame, alongside the one due to the Earth’s motion. As a result, the received signal is dispersed across a frequency range and corrections, aimed at removing the orbital modulation, are therefore required to achieve detection. However, Doppler corrections can, in some cases, significantly vary within the uncertainties with which orbital parameters are known. In order to optimally exploit the constraints drawn from electromagnetic observations we implement a semi-coherent search, more robust than fully coherent methods, in which the coherence time is evaluated for each source taking into account uncertainties in its orbital parameters. This method was tested and applied to a set of twelve targets from the ATNF catalogue. The search identified a single outlier which astrophysical origin has been confidently excluded. For the first time to our knowledge, we then set upper limits on the signal strain from these 12 pulsars, the lowest being $h_{UL} \sim 1.06 \cdot 10^{-25}$ for PSR J1326-4728B.

I. INTRODUCTION

While $\mathcal{O}(10^8 - 10^9)$ neutron stars (NS) are thought to exist in our Galaxy [1], only a few thousand have been observed thanks to their electromagnetic (EM) emission. Most of these are rotation-powered radio pulsars whose emission beam points along our line-of-sight, while a fraction are known from their broadband emission, which can be powered by accretion, dissipation of magnetic energy or even residual thermal energy [2]. Besides their EM emission, rotating NSs are expected to radiate continuous gravitational waves (CWs) if a shape asymmetry is present. CW emission is essentially monochromatic in the NS reference frame and can be driven by elastic, thermal, or magnetic anisotropic stresses in the NS crust or core [3], or from a mass-current quadrupole induced by core fluid instabilities like, e.g., the r -modes [4]. Detecting CW signals will therefore allow us to determine the NS mass quadrupole, hence its degree of asymmetry, and eventually get insights on the NS interior structure as well as on the equation of state (EoS) of matter at supra-nuclear density (see, e.g. [5] and references herein).

All-sky searches for CWs represent to date the only means by which we can unveil the huge pop-

ulation of undetected NS in the Galaxy. These all-sky searches for CWs have already been carried out in Advanced LIGO and Advanced Virgo data from previous science runs, leading to upper limits on the Gravitational Wave (GW) signal strain from NS in the galactic population both for isolated stars [6–9] and in binary systems [10–12].

On the other hand, the EM emission of known NS, both isolated and in binary systems, provides accurate measurements of their sky location, rotational and, eventually, binary orbital parameters. For these sources, searches have been performed looking for a corresponding CW signal [13–23], either using a single-template approach (targeted) or rather exploring a limited range around the known parameters (narrow-band or directed).

In this work we present a novel approach to targeted searches of CWs from known pulsars in binary systems. Uncertainties on the orbital parameters for such systems can sometimes affect the accuracy of Doppler corrections leading to a loss of Signal-to-Noise Ratio (SNR) [24]. To tackle this problem, we adopt a semi-coherent technique in which data are first divided into segments, each of which is analyzed coherently before all segments are finally recombined incoherently. Semi-coherent methods are less sensitive but more robust than single-segment analyses, as they do not rely on a strict phase-coherence of the signal over extended time spans.

^a mail to lorenzo.mirasola@ca.infn.it

The novelty of our method is to choose a customised length of the segments according to the combined uncertainty of the neutron star binary orbital parameters. In this way, we can perform a single-template search and reduce the potential significance loss, even with some reduction in sensitivity.

The method has been tested and then applied on a subset of pulsars from the ATNF catalogue¹ (version 1.70) using O3 data². Although throughout this paper we exploit only our new semi-coherent method, the coherence time calculation highlighted a fraction of the targets for which a full-coherent approach could be safely applied without the need of a grid. Future searches can, in principle, make use of our coherence time calculation to discern which approach is safer for a given ephemeris.

The plan of the paper is as follows: Sec. II describes the adopted phase model for the GW signal, used to remove the Doppler modulation due to the relative motion between the star and detector. Sec. III lists the selection criteria of the chosen pulsars in binary systems as extracted from the ATNF catalogue. Sec. IV outlines the analysis method, together with its validation. A thorough discussion of the results is provided in Sec. V, which also presents the upper limit calculation that we performed. Sec. VI summarises our results and their relevance for future searches, as well as discusses possible future developments.

II. THE EXPECTED SIGNAL

Here, we briefly describe the expected CW signal from a rotating NS, either isolated or in a binary system.

A. Isolated neutron star phase

The signal strain from a non-axis-symmetric NS, which is rotating around one of its principal axes, can be expressed in the detector reference frame [27] as

$$h(t) = h_0 F_+(t; \vec{n}, \Psi) \frac{1 + \cos^2 \iota}{2} \cos \phi(t) + h_0 F_\times(t; \vec{n}, \Psi) \cos \iota \sin \phi(t), \quad (1)$$

where ϕ represents the GW phase (including modulations from the Earth motion) and ι the inclination angle of the NS rotational axis with respect to the line of sight; $F_{+, \times}$ are the time-dependent beam pattern functions [27] that encode the detector response as a function of the source sky position \vec{n} , and of the polarization angle Ψ . The CW amplitude is defined for a quadrupolar deformation as

$$h_0 = \frac{4\pi^2 G}{c^4} \frac{I_{zz} \varepsilon f_{GW}^2}{d}, \quad (2)$$

where $\varepsilon = (I_{xx} - I_{yy}) / I_{zz}$ is the equatorial ellipticity and f_{GW} the signal frequency.

Following [28], Eq.(1) can be expressed as the real part of

$$h(t) = H_0 (A^+ H_+ + A^\times H_\times) e^{j\phi(t)}, \quad (3)$$

where $A^{+/\times} = F^{+/\times}(t; \vec{n}, 0)$, and

$$H_0 = \frac{h_0}{2} \sqrt{1 + 6 \cos^2 \iota + \cos^4 \iota}, \quad (4)$$

$$H_+ = \frac{\cos 2\Psi - j \eta_{\text{pol}} \sin 2\Psi}{\sqrt{1 + \eta_{\text{pol}}^2}}, \quad (5)$$

$$H_\times = \frac{\sin 2\Psi + j \eta_{\text{pol}} \cos 2\Psi}{\sqrt{1 + \eta_{\text{pol}}^2}}, \quad (6)$$

being

$$\eta_{\text{pol}} = -\frac{2 \cos \iota}{1 + \cos^2 \iota} \quad (7)$$

the semi-minor to semi-major axis ratio of the polarization ellipse. In particular, $\eta_{\text{pol}} = 0$ for a linearly polarized wave and $\eta_{\text{pol}} = \pm 1$ for a circularly polarized wave, where the $+$ ($-$) sign refers to counterclockwise (clockwise) direction.

Moreover, the intrinsic signal frequency $f_{\text{GW}}(t)$ slowly decreases over time due to EM- and GW-driven rotational energy losses of the NS, which cause a secular spin-down³. The phase evolution can be expanded in the NS reference frame as

$$\phi^{\text{src}}(\tau) = 2\pi \left[f_{\text{GW}}(\tau - t_{\text{ref}}) + \frac{\dot{f}_{\text{GW}}}{2} (\tau - t_{\text{ref}})^2 + \dots \right], \quad (8)$$

¹ see <http://www.atnf.csiro.au/research/pulsar/psrcat/> for updated versions

² Third observing run of LIGO-Virgo-KAGRA detectors that took place between April 1st 2019 and March 27th 2020 [25, 26]

³ EM-driven spin-down is usually largely dominant in known pulsars

where t_{ref} stands for the reference time, while τ is the time at the source. Since the Earth moves relative to the source, the induced Doppler modulation can be described as a temporal delay between the CW arrival time at the detector, t_{arr} , and τ .

In order to remove the Doppler modulation, we need to relate τ to t_{arr} such that $\phi(t_{\text{arr}}) = \phi^{src}(\tau(t_{\text{arr}}))$. Following Eq.(5) of [15], $\tau(t_{\text{arr}})$ can be written for an isolated NS as

$$\tau(t_{\text{arr}}) = t_{\text{arr}} + \frac{\vec{r}_{\text{SSB}} \cdot \vec{n}}{c} - \Delta_E - \Delta_S - \frac{D}{c}, \quad (9)$$

where the second term is the Rømer delay due to the Earth's motion, being \vec{r}_{SSB} the vector from the Solar System Barycenter (SSB) to the detector. It represents the vacuum delay between the arrival time at the observatory and the SSB. The third contribution is given by the Einstein delay (Δ_E), which takes into account the redshift due to the other solar system bodies. The term Δ_S is the Shapiro delay, linked to the deflection of a signal passing close to the Sun. The last term is the vacuum travel time related to the distance D between the SSB and the source. Following [15], this last term can be neglected by redefining the intrinsic spin-down parameters.

B. Binary motion phase

The NSs in binary systems represent a more challenging target since their orbital motion induces an additional Doppler effect that must be accounted for in the analysis. The orbital motion is parameterized as a time-dependent delay added to Eq. (9),

$$\tau_{\text{bin}} = \tau(t_{\text{arr}}) - \frac{R(\tau_{\text{bin}})}{c} - \Delta_E^{\text{bin}} - \Delta_S^{\text{bin}}, \quad (10)$$

where Δ_E^{bin} and Δ_S^{bin} are, respectively, the Einstein and Shapiro delay due to the binary companion and to possible bodies in the system [29, 30]. Finally, R/c represents the Rømer delay of the binary system, with $R(\tau_{\text{bin}})$ being the radial distance of the CW-emitting NS from the *Binary Barycenter* (BB), projected along the line of sight.

Following the discussion in [15, 24], R/c can be expressed in terms of five binary orbital parameters: a_p , the projected semi-major axis along the line of sight normalised to c ; P_{orb} , the orbital period; e , the orbit eccentricity; ω , the argument of periastron; and t_p , the time of periastron passage. Therefore, the binary delay is given by

$$\frac{R}{c} = a_p \left[\sin \omega (\cos E - e) + \cos \omega \sin E \sqrt{1 - e^2} \right], \quad (11)$$

where E is the eccentric anomaly, expressed through the Kepler's equation

$$\tau_{\text{bin}} - t_p = \frac{P_{\text{orb}}}{2\pi} (E - e \sin E). \quad (12)$$

In the regime $a_p \ll P_{\text{orb}}$, which is normally the case for the observed systems, we can use the additional approximation of $E(\tau) \approx E(t)$ as the change in E during the time R/c will be negligible. As a consequence, defining $t \equiv \tau(t_{\text{arr}})$, $E(t)$ becomes

$$t - t_p \approx \frac{P_{\text{orb}}}{2\pi} (E - e \sin E). \quad (13)$$

Moreover, since eccentricity tends to be dissipated with time, it is useful for relatively old binary pulsars to expand Eq.(11) in the small eccentricity regime up to the leading order in e . The binary Rømer delay can be written as [24]

$$\frac{R}{c} \approx a_p \left[\sin \psi(t) + \frac{\kappa}{2} \sin 2\psi(t) - \frac{\eta}{2} \cos 2\psi(t) - \frac{3}{2} \eta \right], \quad (14)$$

where η, κ represent the *Laplace-Lagrange* parameters, and $\psi(t)$ is the mean anomaly measured with respect to the time of ascending node t_{asc} . Defining the mean orbital angular velocity $\Omega = 2\pi/P_{\text{orb}}$, the mentioned parameters can be expressed as

$$\begin{aligned} \kappa &= e \cdot \cos \omega, & \eta &= e \cdot \sin \omega, \\ \psi(t) &= \Omega (t - t_{\text{asc}}), & t_{\text{asc}} &= t_p - \frac{\omega}{\Omega}. \end{aligned} \quad (15)$$

III. TARGET SELECTION

Our analysis was carried out on a subset of pulsars in binary systems from version 1.70 of the ATNF catalogue [31]. We selected targets for which the NS spin period reference time was within the O3 run and for which $\dot{f} \neq 0$. This selection is justified to avoid less precise and potentially incorrect extrapolated values of the source parameters. At the same time, the spin-down condition is required for a CW emission. A list of our selected targets and their parameters of interest is given in Tab.I.

The ephemerides are obtained by fitting the Time of Arrival (ToA) of photons emitted by a pulsar. To

do so, astronomers exploit a time model that, in the case of pulsars in binary system, is constituted either by $(a_p, P_{\text{orb}}, e, \omega, t_p)$, or $(a_p, P_{\text{orb}}, \eta, \kappa, t_{\text{asc}})$ when the eccentricity is small.⁴

IV. ANALYSIS METHOD

Since the binary delay correction can strongly depend on the orbital parameters, a slight offset from the true values can rapidly lead to a substantial loss of phase-coherence, with a consequent loss of SNR (see, e.g., [24]). For this reason, a semi-coherent approach, where the uncertainties on the parameters are taken into account can be mandatory rather than a single-template full-coherent search. Although, the reliability of the method leads to a sensitivity loss (see Eq.(72-73) from [34]) as

$$\frac{h_{\text{sens}}^{(\text{semi-coh})}}{h_{\text{sens}}^{(\text{coh})}} = \left(\frac{T_{FFT}}{T_{\text{obs}}} \right)^{1/4} \quad (17)$$

which is about 23% for $T_{\text{obs}} = 1$ yr and $T_{FFT} = 1$ d. With this rough estimate, the semi-coherent approach is four times worse in sensitivity than a fully coherent approach; however, the real estimation can be more complicated than that, as the sensitivity depends also on the number of selected outliers and the exploited detection statistic, see e.g. [34].

Our method makes use of calibrated and cleaned detector data [35]. We propose the following semi-coherent search: for each of our targets, we first perform a Doppler correction in the time domain with the ephemeris central values, and then we divide the data into chunks of duration T_{FFT} , the so-called coherence time: its evaluation, based on the binary parameters and their uncertainties, is a crucial step of this analysis that we detail in Sec. IV A.

Each chunk is windowed to reduce the finite length effect and then Fourier transformed. The next step is the selection of the local maxima from the equalized spectrum⁵ of the Fourier-transformed chunk [34, 36]: a frequency bin of this spectrum is selected only if its height exceeds a particular threshold $\theta_{\text{thr}} = 2.5$.

As demonstrated in [34], θ_{thr} is linked to the False Alarm Probability (FAP) per chunk p_0 through the relation

$$p_0 = e^{-\theta_{\text{thr}}} - e^{-2\theta_{\text{thr}}} + \frac{1}{3}e^{-3\theta_{\text{thr}}}, \quad (18)$$

that, for our threshold, corresponds to a value of $\approx 7.6\%$.

After that, those selected peaks along the observing run are collected together in a time-frequency map that we call *peakmap*.

The peakmap is then projected onto the frequency axis and the loudest peak around the expected frequency, in the range $f_{\text{GW}} \pm 5\delta f$ ⁶ is selected as a *candidate*, where δf is the Fourier transform frequency resolution given by

$$\delta f = \frac{1}{T_{FFT}}, \quad (19)$$

being T_{FFT} the coherence time.

Then the *Critical Ratio* (CR), which is our detection statistics [34], is evaluated for the chosen candidates as

$$CR = \frac{x - \mu}{\sigma}, \quad (20)$$

where x is the candidate's number of counts in the projection of the peakmap (i.e. the number of times in which that specific bin has been selected in the peakmap), μ and σ are, respectively, the peakmap projection's average and standard deviation calculated outside the region from which the loudest peak is selected. The CR is then used to assess the statistical relevance of the candidate.

An example of a peakmap before and after applying the Doppler correction is shown in Fig.1, where a *Software Injection* (SIs, i.e. simulated signal) was performed in LIGO Livingston (LL) O3 real data.

A. Coherence time evaluation

The frequency shift due to the orbital motion can be linked to the time derivative of Eqs. (11-14) as [15]

$$\frac{\Delta f_{\text{GW}}^{\text{Doppl}}}{f_{\text{GW}}}(t) = \frac{\dot{R}}{c}(t), \quad (21)$$

⁴ For reproducibility, we refer that the ATNF ephemerides mistakenly reported some parameters. We found, in the reference paper [32], seven pulsars for which the ATNF t_p was, instead, the t_{asc} : J1811-0624, J1813-0402, J1824-0621, J1912-0952, J1929+0132, J2001+0701, J2015+0756. While for an eighth pulsar, J2338+4818, the t_p value was reported as t_{asc} [33].

⁵ ratio between the squared modulus of the Fourier-transformed chunk and the average single-sided *Power Spectral Density* [35].

⁶ The choice of 5 bins around f_{GW} is done to allow frequency shifts linked to a residual Doppler modulation due to the offset in the orbital parameters and has been tuned through the injection of fake signals in real data

Name	P_{orb} [day]	a_p [lt-s]	e/η^*	ω [deg] / κ^*	t_p [MJD]	t_{asc} [MJD]
J1326-4728B	0.08961121(1)	0.021455(7)	$1(6)\cdot 10^{-4}^*$	$-4(6)\cdot 10^{-4}^*$	-	58768.037243(4)
J1801-0857B	59.836454(1)	33.87543(1)	$3.82258(7)\cdot 10^{-2}$	302.1086(6)	54757.72304(9)	-
J1811-0624	9.38782916(5)	6.561124(2)	$-3.8(5)\cdot 10^{-6}^*$	$-2.61(12)\cdot 10^{-5}^*$	-	58692.1778781(8)
J1813-0402	10.560352898(4)	9.4263516(5)	$-2.91(17)\cdot 10^{-6}^*$	$-2.97(12)\cdot 10^{-6}^*$	-	58716.88174915(15)
J1823-3021G	1.54013654(5)	3.00331(2)	$3.80466(6)\cdot 10^{-1}$	146.721(1)	58909.681498(8)	-
J1824-0621	100.91365361(5)	44.103911(2)	$-22.809(2)\cdot 10^{-5}^*$	$-2.363(2)\cdot 10^{-5}^*$	-	58734.9698712(18)
J1835-3259B	1.19786323(1)	1.430841(6)	$-2.7(4)\cdot 10^{-5}^*$	$-2.2(3)\cdot 10^{-5}^*$	-	58866.2655109(6)
J1912-0952	29.4925321(5)	5.379447(7)	$-1.62(18)\cdot 10^{-5}^*$	$4.6(3)\cdot 10^{-5}^*$	-	58685.963815(4)
J1929+0132	9.265037044(4)	8.2675144(6)	$-8.12(18)\cdot 10^{-6}^*$	$-2.44(18)\cdot 10^{-6}^*$	-	58757.4798650(2)
J2001+0701	5.22708263(2)	2.23028000(15)	$-1.85(12)\cdot 10^{-5}^*$	$1.29(12)\cdot 10^{-5}^*$	-	58754.681385(11)
J2015+0756	6.456719142(2)	5.1642574(2)	$-1.3(1)\cdot 10^{-6}^*$	$2.80(13)\cdot 10^{-6}^*$	-	58780.4740740(2)
J2338+4818	95.25536(2)	117.58572(7)	$1.8237(9)\cdot 10^{-3}$	99.65(2)	58868.444(7)	-

Table I. List of selected targets from the 1.70 ATNF catalogue version. The starred values refer to the low-eccentricity parameters η and κ , see Eq.(15), used during the analysis. A description of the binary orbital parameter is given in Sect.II B.

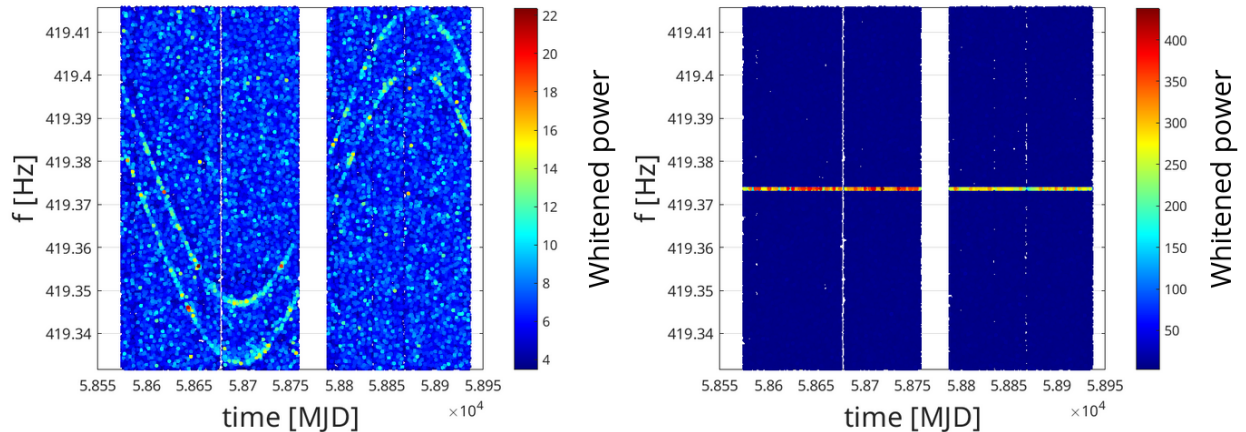


Figure 1. Peakmaps of a fake signal injected with $h_0 = 10^{-24}$ into real LL data from the O3 run over a timespan of ~ 1 yr, without (*left*) and with (*right*) the Doppler correction. The signal mimics that expected from J1326-4728B, i.e., with the same binary orbital parameters and the same sky position, while the injected frequency is $f_{GW} = 2f_{rot} + 2$ Hz to avoid the overlap with a possible true signal.

where

$$\frac{\dot{R}}{c} = a_p \Omega \frac{\cos \omega \cos E \sqrt{1 - e^2} - \sin \omega \sin E}{1 - e \cos E}, \quad (22)$$

not having considered time derivatives of the orbital parameters, as their variations are typically negligible on the characteristic observing run's duration of $T_{obs} \sim 1$ yr.

In the limit of low eccentricities, Eq. (22) can be expressed as [24]

$$\frac{\dot{R}}{c} \approx a_p \Omega (\cos \psi + \kappa \cos 2\psi + \eta \sin 2\psi). \quad (23)$$

We evaluate the coherence time of the targets re-

quiring that the maximum⁷ frequency shift caused by uncertainties on the Doppler correction (i.e., the variation of Δf_{GW}^{Dopp1} with respect to the parameters) must be confined in a single frequency bin.

We calculate the residual Doppler modulation as

$$\delta \Delta f_{GW}^{Dopp1}(t) = f_{GW} \cdot \sum_{i=1}^5 \left. \frac{\partial \dot{R}/c}{\partial x_i} \sigma_{x_i} \right|_{x_i=x_0}, \quad (24)$$

where x_i are the orbital parameters (see Sec. III and Tab. I), σ_{x_i} their uncertainties, and x_0 their central values as given in the ephemerides. For the sake

⁷ selected along the observation time

of completeness, we detail the calculation of Eq.(24) in App.A.

The coherence time of each source can then be estimated as

$$\max \left(\left| \delta \Delta f_{GW}^{\text{Doppl}}(t) \right| \right)_{t \in T_{\text{obs}}} \leq \delta f, \quad (25)$$

where δf is given in Eq.(19).

Finally, in the left plot of Fig.2, we report the T_{FFT} of the targets in Tab.I calculated with Eq.(25). We do not evaluate $\delta \Delta f_{GW}^{\text{Doppl}}(t)$ using a squared sum as it would not capture potential anticorrelation among the orbital parameters, conservatively lowering the coherence time. For those targets for which the high eccentricity parameters are given (see Tab.I), our estimation with Eq.(24) is higher up to a factor of 5 than the squared sum calculation, being less conservative and potentially more sensitive. This choice is supported by the tests in Sec.IV C and App.C that did not highlight strong SNR losses linked to the offset in the orbital parameters. On the other hand, when the low eccentricity parameters are given, our coherence time estimation is up to a factor 1.8 lower than the squared sum ones, meaning that we are more conservative in that scenario at the price of sensitivity loss (see Eq.(17)). Although in this work we describe a semi-coherent approach, the coherence time calculation shows that a fraction of targets can be safely studied with a fully coherent approach as $T_{FFT} > T_{\text{obs}}^{O3} \sim 1$ yr and assuming that the uncertainties on binary parameters are the dominant ones.

However, T_{FFT} cannot be longer than about one sidereal day⁸ as a dedicated semi-coherent technique for the peakmap that includes the S_{FFT} statistic [37] has just been developed for the isolated pulsars science case. When T_{FFT} approaches T_{sid} , a CW monochromatic signal is split into five peaks at $f_{GW} \pm k/T_{\text{sid}}$, with $k = 0, 1, 2$, due to the harmonic components of the beam pattern function [27], with a significant loss in the sensitivity if not kept into account. While we foresee the implementation of

the S_{FFT} statistic in the future, the present analysis is conservatively performed with a maximum coherence time equal to

$$T_{FFT}^{\text{max}} = \frac{1}{5} \cdot T_{\text{sid}} \approx 17230 \text{ s}, \quad (26)$$

for all our targets, since $T_{FFT} > T_{FFT}^{\text{max}}$ (see Fig.2). This value has been set after the tests reported in App.B, where we observe a loss in significance for higher coherence times.

We would like to remark that despite we are not able to reach the estimated coherence times, lower T_{FFT} are always more reliable against the offset in the orbital parameter. In that sense, our method is complementary to full-coherent ones that exploit a grid [19] or not [18] around the measured parameters, or parallel to other semi-coherent pipelines such as [14]. In addition to that, the peculiarity of this work is that it allows to perform a single Doppler correction at the ephemeris central parameters. This is computationally very convenient compared with other pipelines [14], where a grid around the estimated values is built to probe the parameter space. Indeed, if σ_{par} (i.e., the uncertainty on a binary orbital parameter) is taken as a grid step, an interval of $\pm n_{\sigma} \sigma_{\text{par}}$ around each parameter becomes challenging even for small n_{σ} , since in each dimension we would explore in the worst case $(2n_{\sigma} + 1)$. Hence, since the dimensionality of the binary parameter space is 5, the total number of points would be $N_{\text{grid}} = (2n_{\sigma} + 1)^5$ values. Finer grids will be even more computationally challenging to scale towards larger pulsar datasets.

B. Sensitivity estimation

Following the conservative sensitivity estimation of [34], we can evaluate the expected minimum detectable strain (at a given Confidence Level Γ , CL), which would produce a candidate in a fraction $\geq \Gamma$ of a large number of repeated experiments, as

$$h_{\text{sens}} \approx \frac{4.02}{N_{FFT}^{1/4} \varepsilon^{1/4} \theta_{\text{thr}}^{1/2}} \sqrt{\frac{S_n(f)}{T_{FFT}}} \left(\frac{p_0(1-p_0)}{p_1^2} \right)^{1/4} \sqrt{CR_{\text{thr}} - \sqrt{2} \text{erfc}^{-1}(2\Gamma)} \propto \left(\frac{1}{T_{\text{obs}} T_{FFT}} \right)^{1/4}, \quad (27)$$

where $S_n(f)$ is the unilateral noise spectral density,

⁸ The sidereal day represents the time taken by Earth to complete a full rotation around its rotational axis with respect to the stars. $T_{\text{sid}} \sim 86164$ s.

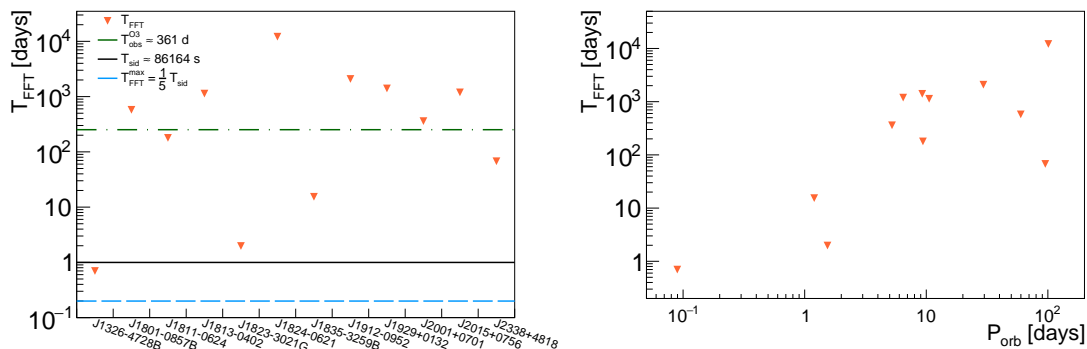


Figure 2. (left) Coherence time of each of the targets reported in Tab.I according to Eq.(25). The sidereal day duration as well as the O3 duration are reported for comparison as the solid black line and dashed-dotted green one, respectively. The dashed one is the upper value of $\frac{1}{5} \cdot T_{sid}$ used in this work to avoid the five peaks splitting. (right) Coherence times plotted against the orbital period of the targets.

$$p_1 = e^{-\theta_{thr}} - 2e^{-2\theta_{thr}} + e^{-3\theta_{thr}}, \quad (28)$$

p_0 is given in Eq.(18), ε is the duty cycle of the considered detector [38], and $\text{erfc}(x)$ is the complementary error function defined as $\text{erfc}(x) = \frac{2}{\sqrt{\pi}} \int_x^{+\infty} e^{-t^2} dt$. The curves presented throughout this paper consider $CR_{thr} = 5$, which corresponds to a False Alarm Probability (FAP) in the case of white noise only of about $2.87 \cdot 10^{-7}$ [34], $\theta_{thr} = 2.5$ [34], $\Gamma = 95\%$, and the number of chunks N_{FFT} is given by

$$N_{FFT} = \frac{T_{obs}}{T_{FFT}}. \quad (29)$$

Since h_{sens} is proportional to $(T_{obs} \cdot T_{FFT})^{-1/4}$, the higher the T_{FFT} , the better is the sensitivity. Hence, longer coherence times are preferred to shorter ones.

C. Test on injected signals

The computational efficiency of our new method relies on a single Doppler correction applied to each target, without the need to scan across a grid in parameter space set by the uncertainty on orbital parameters. As a test, a set of $2 \cdot 10^3$ SIs for each of the targets in Tab.I was injected into LL real O3 data [39]. All the SIs mimicked the GW signal coming from the targets with randomly distributed binary parameters around the central ephemeris values, while the Doppler correction was performed at the ephemeris ones in order to study the influence of the offset on the signal reconstruction.

Each SI set is injected with $f_{GW} = 2f_{rot} + 2$ Hz and fixed amplitude at $h_0 = h_{sens}$ (see Eq. 27). We introduced a frequency offset of 2 Hz to avoid overlapping the simulated signal with a possible true signal coming from the same target.

The SI binary parameters are randomly picked for each injection from Gaussians centred at the ephemeris values, using as standard deviation their uncertainties. The remaining parameters are picked from flat distributions as follows: $\cos \iota \in [-1, 1]$, and $\Psi \in [-45^\circ, 45^\circ]$. Lastly, the beam pattern function is evaluated at the provided sky position.

For each injection we perform a Doppler correction adopting the ephemeris central values given in the ATNF catalogue. Their uncertainties are accounted for by our specifically designed choice of T_{FFT} (Eq. 25), which ensures phase-coherence is maintained within each data segment. After this step, the peakmap is created using the chosen T_{FFT} , and then projected to evaluate the CR (Eq.20) of the loudest peak around f_{GW} .

Fig. 3 shows the CR of the SI test for each of the selected targets against $\cos \iota$. As a reference, we infer empirically the same distribution when no offset is introduced in the orbital parameters by injecting 100 SIs with random $\Psi \in [-45^\circ, 45^\circ]$, while $\cos \iota$ is fixed to probe the entire interval $[-1, 1]$. We do not find any remarkable differences between the two distributions.

As an additional step of the method's validation we artificially enlarged the uncertainties on two pulsars (J1326-4728B and J1823-3021G) by an order of magnitude and repeated the test presented in this section with $T_{FFT} < T_{FFT}^{max}$. The outcome, which did not highlight again a CR dependence on the offset, is reported in App.C.

Overall, we can conclude that this method can

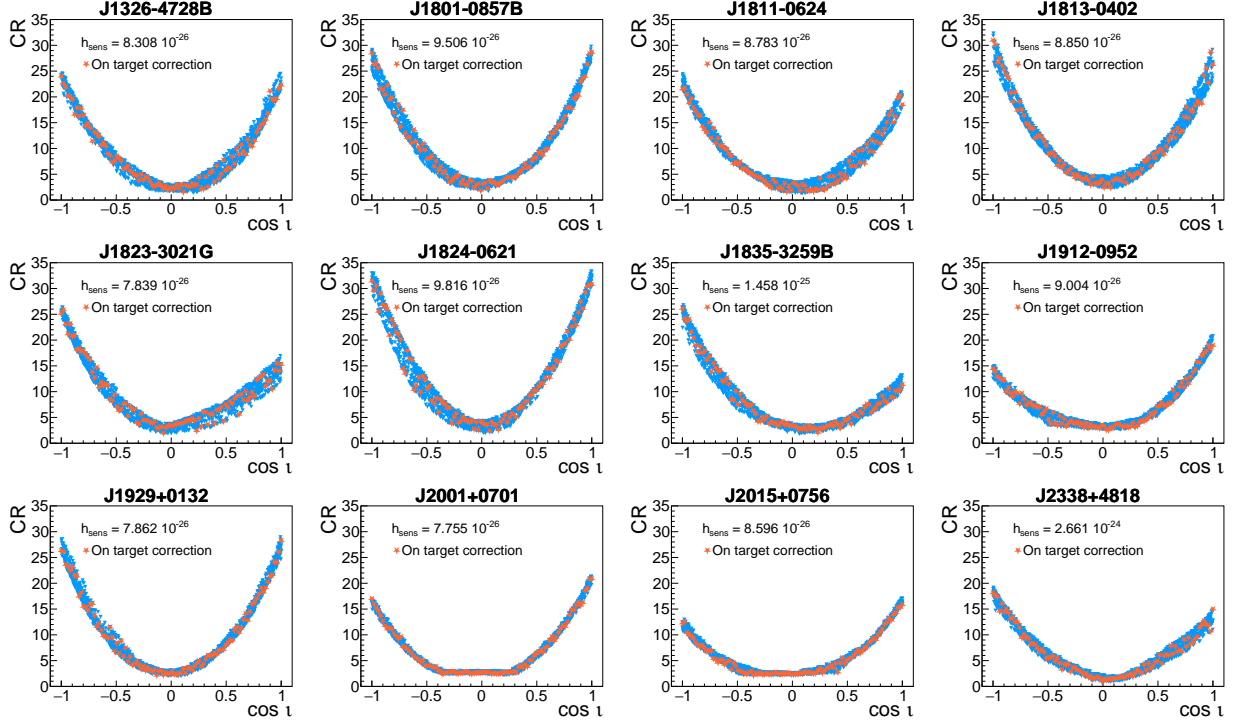


Figure 3. CR plotted against $\cos \iota$ for each of the target in Tab.I of the $2 \cdot 10^3$ SIs set. Each of the SI emulates the target’s sky positions but random binary orbital parameters according to the measured values and their uncertainties. The Doppler correction is then performed with the central ephemeris values in order to study the offset’s influence on the CR. We plot an empirical CR distribution when the demodulation is performed using the injected parameters (“on target” in the plot). We refer the reader to Sec.IV C for a thorough description of the test.

safely perform a single Doppler correction at the ephemeris central values, without the need for a grid thus saving computing time at a reasonable sensitivity loss.

V. RESULTS

Finally, the search method has been applied to both LL and LIGO Hanford (LH) O3 real data [39]. Virgo and KAGRA data are not included in the analysis as their sensitivities are worse in the analysed frequency bands.

Based on the test with the SIs reported in Sec.IV C, for the targets considered here, we can safely perform a single Doppler correction at the ephemeris central values.

The threshold to identify potentially interesting outliers has been set at $CR_{thr} = 5$. In this work, we found a single outlier with $CR > CR_{thr}$, see Fig.4, for pulsar J2338+4818, which is likely of terrestrial origin. Indeed, comparing the peakmap with and without the Doppler correction, a clear persistent excess power, linked to a calibration line, is present, see Fig.5. The procedure to select a candidate is

as in Sec.IV but since no CW-related one has been found, we computed the Upper Limits (ULs) for all the pulsars through an injection campaign in LL and LH data.

The calculation proceeds similarly as in [40] with the difference that we incorporate the binary modulation. We inject one by one a set of 100 SIs into the LL and LH full O3 data with a frequency close to the target’s one, and we start from a strain amplitude of $H_0 = 0.75 \cdot h_{sens}$, being the factor 0.75 due to the averaged nature of the h_{sens} calculation (see [34] and Eq.(27)), hence the UL for a specific pulsar can be underneath the sensitivity curve. Following the test method (see Sect.IV), we inject each SI with random orbital parameters taken from Gaussians around the ephemeris central values, while the Doppler correction is performed with the central ones. As previously mentioned, the frequency of the SIs is taken to be outside the signal region (i.e., the region where the candidate’s peak is selected) to avoid overlap. If 95% of the signals are not producing $CR \geq CR_{thr}$,

⁹ In the case of the outlier in LL data, the UL is calculated with the measured CR

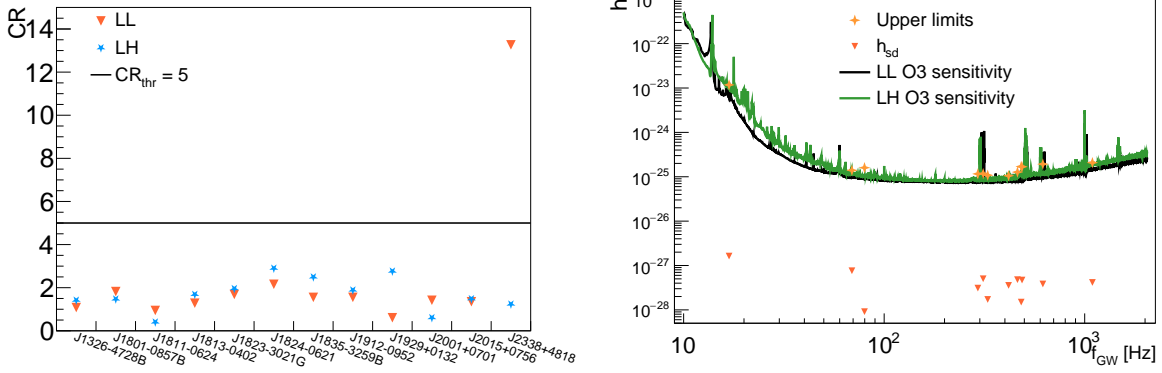


Figure 4. (*left*) Critical ratio obtained for each of the targets reported in Tab.I after performing the Doppler correction at the ephemeris central values. A single outlier, i.e. $CR > CR_{thr}$, have been found, for pulsar J2338+4818 that has a likely instrumental origin, related to a close calibration line, see Fig.5. (*right*) ULs on the target strains calculated through the injection of fake signals at the 95% CL in real data (ocher diamonds). The ULs are compared with the spin-down limits (see Eq.(31)) of the targets (orange triangles), and the estimated sensitivity curves for LL and LH are calculated again with Eq.(27).

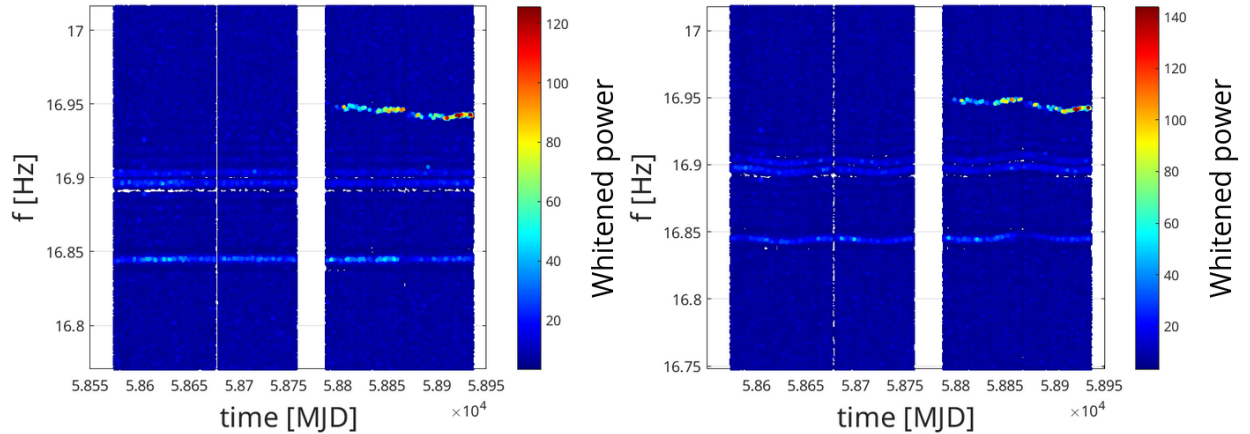


Figure 5. Peakmaps of the LL detector before (*left*) and after (*right*) Doppler correction for the pulsar J2338+4818. The search highlighted an outlier (see Fig.4) that is likely to be of instrumental origin, due to a persistent line at $f \sim 16.85$ Hz.

another set of SIs is injected with a strain increased by $h_{sens}/10$. This process is repeated till the condition is satisfied, and, in that case, the UL for the single detector is found to be

$$h_{UL}^{idet} \approx 1.31 \cdot H_{0UL}^{idet}, \quad (30)$$

being H_{0UL}^{idet} the H_0 single detector's UL, while the factor 1.31 comes from averaging Eq.(4) over a flat $\cos \iota$ distribution. Then, we choose the highest UL between the two detectors as the UL for the single target. Our ULs are presented on the right of Fig.4 and are compared with the expected sensitivity curves for LL and LH (see Eq.(27)) and the spin-down limit defined as

$$h_{sd} = \frac{1}{D} \sqrt{\frac{5G}{4c^3} I_{zz} \left(-\frac{\dot{f}_{GW}}{f_{GW}} \right)} \quad (31)$$

for a NS with moment of inertia $I_{zz} = 10^{38}$ kg m².

VI. CONCLUSION

In this paper, we have described a new semi-coherent method that is highly computationally efficient to search for CW signals from known pulsars in binary systems. These targets can be more challenging to study as the binary Doppler correction

can rapidly change within the binary orbital parameter uncertainties, potentially reducing the SNR.

The efficiency of the method here shown is a combination of two aspects: a custom optimization of the coherence time to reduce the power loss and increase the detection chances; and a single Doppler correction to assess the presence of a signal, drastically reducing the needed computational cost.

Independently on the method, our coherence time calculation can be of crucial relevance for future targeted searches where NS in binary systems are involved. With our calculation, we have given a quantitative estimate to understand whether a pulsar can be safely studied with a single-template fully coherent approach or a grid has to be built around the orbital parameters.

The coherence time is evaluated with the ephemeris binary orbital parameters and their uncertainties, requiring that the variation of the Doppler effect must be confined in a single frequency bin. Applying this method to twelve targets from the ATNF catalog version 1.70, we found coherence times that span several orders of magnitudes, from ~ 0.7 d, up to ~ 30 yr.

We successfully tested the method by injecting $2 \cdot 10^3$ simulated signals, mimicking each of the twelve ATNF targets, in LIGO-Livingston O3 real data. Each signal was injected drawing random orbital parameters from Gaussian distributions built around the measured values; then, a Doppler correction was performed using the ephemeris central values to study the signal reconstruction. The test did not highlight a strong dependence of the SNR on the offset between the injected parameters and those used for the Doppler correction.

In order to achieve better sensitivities longer coherence times are needed. We have already foreseen crucial improvements from the software side that will overcome the sidereal day that is now limiting the present one.

By applying the method to look for a real CW coming from the selected targets, we have found a single outlier that we asses of terrestrial origin. We then computed upper limits on the gravitational wave strain amplitude of these targets for the very first time to our knowledge, through the injections of fake signals into real data.

Appendix A: Binary Doppler variation

As described in Sec.IV, our coherence time calculation relies on the variation of the orbital Doppler expressed by Eq.(24). Here we detail its calculation. As mentioned in Sec.III, ephemerides are given with either the parameters $(a_p, P_{\text{orb}}, e, \omega, t_p)$, or

$(a_p, P_{\text{orb}}, \eta, \kappa, t_{\text{asc}})$.

Let us now focus singularly on each of the cases.

1. Low eccentricity regime

We use the low eccentricity approximation (see Eq.(14)) whenever η, κ and t_{asc} are given or the eccentricity is lower than 0.1 [24]. Since in the former scenario η, κ and t_{asc} are calculated using other parameters (see Eqs.(15)-(16)), the Doppler variation will have to keep that into account.

Let us start from the common term given by the derivative of Eq.(23) with respect to a_p

$$\frac{\partial \dot{R}/c}{\partial a_p} = \frac{1}{a_p} \cdot \frac{\dot{R}}{c}. \quad (\text{A1})$$

Considering the scenario where the lagrangian parameters are given, the contributions from the other parameters are calculated as

$$\frac{\partial \dot{R}/c}{\partial P_{\text{orb}}} = \frac{1}{P_{\text{orb}}} \left(a_p \Omega \psi (\sin \psi + 2\kappa \sin 2\psi - 2\eta \cos 2\psi) - \frac{\dot{R}}{c} \right), \quad (\text{A2})$$

$$\frac{\partial \dot{R}/c}{\partial t_{\text{asc}}} = a_p \Omega^2 (\sin \psi + 2\kappa \sin 2\psi - 2\eta \cos 2\psi), \quad (\text{A3})$$

$$\frac{\partial \dot{R}/c}{\partial \eta} = a_p \Omega \sin 2\psi, \quad (\text{A4})$$

$$\frac{\partial \dot{R}/c}{\partial \kappa} = a_p \Omega \cos 2\psi. \quad (\text{A5})$$

The contributions are calculated differently if e, ω, t_p are given

$$\frac{\partial \dot{R}/c}{\partial P_{\text{orb}}} = -\frac{1}{P_{\text{orb}}} \left(a_p \Omega (\omega - \psi) (\sin \psi + 2\kappa \sin 2\psi - 2\eta \cos 2\psi) + \frac{\dot{R}}{c} \right), \quad (\text{A6})$$

$$\frac{\partial \dot{R}/c}{\partial t_p} = \frac{\partial \dot{R}/c}{\partial t_{\text{asc}}}, \quad (\text{A7})$$

$$\frac{\partial \dot{R}/c}{\partial e} = a_p \Omega (\cos 2\psi \cos \omega + \sin 2\psi \sin \omega), \quad (\text{A8})$$

$$\frac{\partial \dot{R}/c}{\partial \omega} = -a_p \Omega (\sin \psi + 2\kappa \sin 2\psi - 2\eta \cos 2\psi). \quad (\text{A9})$$

2. High eccentricity regime

On the other hand, the Doppler variation in the high eccentricity regime is calculated by exploiting

the following contributions

$$\frac{\partial \dot{R}/c}{\partial E} = \frac{a_p \Omega (\sin \omega (e - \cos E) - \cos E \sin \omega \sqrt{1 - e^2})}{(1 - e \cos E)^2} \quad (\text{A10})$$

$$\frac{\partial \dot{R}/c}{\partial P_{\text{orb}}} = -\frac{\Omega}{P_{\text{orb}}} \frac{\partial \dot{R}/c}{\partial E} \frac{t - t_p}{1 - e \cos E}, \quad (\text{A11})$$

$$\frac{\partial \dot{R}/c}{\partial t_p} = -\frac{\Omega}{1 - e \cos E} \frac{\partial \dot{R}/c}{\partial E}, \quad (\text{A12})$$

$$\begin{aligned} \frac{\partial \dot{R}/c}{\partial e} = & \frac{\sin E}{1 - e \cos E} \frac{\partial \dot{R}/c}{\partial E} + \frac{a_p \Omega}{(1 - e \cos E)^2} \left(\cos E \left(\frac{\cos E - e}{\sqrt{1 - e^2}} \cos \omega - \sin \omega \sin E \right) + \right. \\ & \left. + \sin^2 E \frac{\sin \omega (e - \cos E) - \cos \omega \sin E \sqrt{1 - e^2}}{\sin E - \cos E (E - \Omega (t - t_p))} \right), \end{aligned} \quad (\text{A13})$$

$$\frac{\partial \dot{R}/c}{\partial \omega} = \frac{a_p \Omega}{1 - e \cos E} (\sin \omega \cos E \sqrt{1 - e^2} + \cos \omega \sin E). \quad (\text{A14})$$

As expressed in Eq.(24), the Doppler variation consists of the sum of the terms listed in this appendix, weighted by the uncertainty on each parameter.

Appendix B: Upper bound to the coherence time

The current implementation of the method presented in Sec.IV does not account for the Earth's rotational Doppler. Due to the harmonic components of the beam pattern function [27], the power of the monochromatic CW is split into up to five components at $f_{GW} \pm k/T_{sid}$, with $k = 0, 1, 2$, limiting the coherence time of a search if not correctly kept into account.

Since the relative height of the harmonics is not constant but rather depends on the detector and source locations [41], the splitting is not uniform and rules the number of peaks found above the noise level.

We set the highest coherence time of the search by studying the worst-case scenario, where the splitting is almost even among the harmonics. In the top part of Fig.6 we show the power spectrum of the *Hardware Injection*¹⁰ (HI) 1 and an isolated NS SI, we report the injections' parameters in Tab.II, where five and four harmonics are visible respectively after removing all the Doppler modulation except the

sidereal one. We analyse both the signals with different coherence time in $T_{FFT} \in [0.02 T_{sid}, T_{sid}]$ with a step of $0.05 T_{sid}$. The bottom plot in Fig.6 shows the CR obtained with each of the T_{FFT} values. We observe a decreasing trend for both the SI and HI1 that starts around $T_{FFT} \sim 0.2 T_{sid}$ confirming this effect can significantly reduce the detection chances if not properly accounted for. For this reason, we set $0.2 T_{sid}$ as our highest coherence time.

	HI 1	SI
α	37.39°	121.98°
δ	-29.45°	-21.49°
f_{GW} [Hz]	848.937	101.217
\dot{f}_{GW} [Hz/s]	$-3 \cdot 10^{-10}$	0
h_0	$1.68 \cdot 10^{-24}$	$2.74 \cdot 10^{-25}$
$\cos \iota$	0.46	0.34
Ψ	20.40°	-28.60°

Table II. Injection parameters of the signals shown in Fig.6. The frequency reference time is given at $t_{\text{ref}} = 58574$ MJD.

Appendix C: Test with larger error bars

As discussed in Sec.IV A, the test of the method and the analysis have been carried out using $T_{FFT} = T_{sid}/5$ as the sidereal day duration represents a burden for the present implementation.

As a further test, we artificially enlarged the uncertainties of all the orbital parameters by an order of magnitude for J1326-4728B and J1823-3021G (the two pulsars with the lowest estimated coherence

¹⁰ CW injected through the detector hardware for testing purposes, see [here](#) for the injection parameters

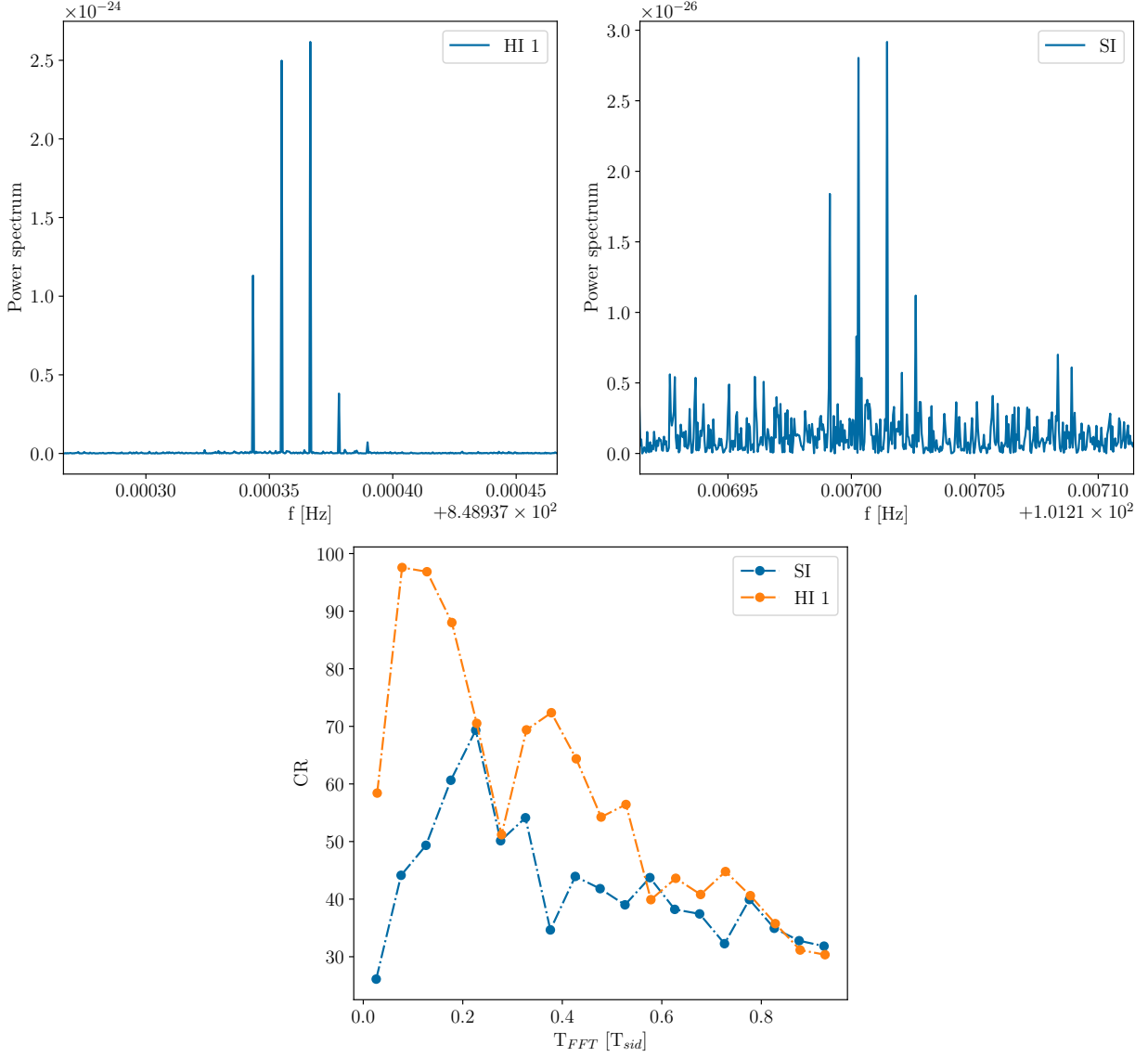


Figure 6. (*top*) Power spectra of the HI 1 and a SI for which the 5 harmonics of the signals are visible, see Tab.II for the injection parameters. (*bottom*) CR as a function of the coherence time. Too high values tend to disperse the signal power, lowering the significance of the candidate.

time in Fig.2, refer to Tab.I for the uncertainties). Since Eq.(24) depends linearly on the uncertainties, the equivalent coherence time is reduced by a factor of 10 w.r.t. the nominal scenario.

Hence, we have repeated the test in Sec.IV C using the increased errors and coherence times

$$T_{FFT}^{J1326-4728B} = 6004 \text{ s}, \quad T_{FFT}^{J1823-3021G} = 16212 \text{ s},$$

which are, now, both below T_{FFT}^{max} . The test outcome is shown in Fig.7. As in Fig.3, we are not observing a significant loss of detection statistic linked to the residual Doppler.

ACKNOWLEDGMENT

This research has made use of data or software obtained from the Gravitational Wave Open Science Center (gwosc.org), a service of the LIGO Scientific Collaboration, the Virgo Collaboration, and KAGRA. This material is based upon work supported by NSF's LIGO Laboratory which is a major facility fully funded by the National Science Foundation, as well as the Science and Technology Facilities Council (STFC) of the United Kingdom, the Max-Planck-Society (MPS), and the State of Niedersachsen/Germany for support of the

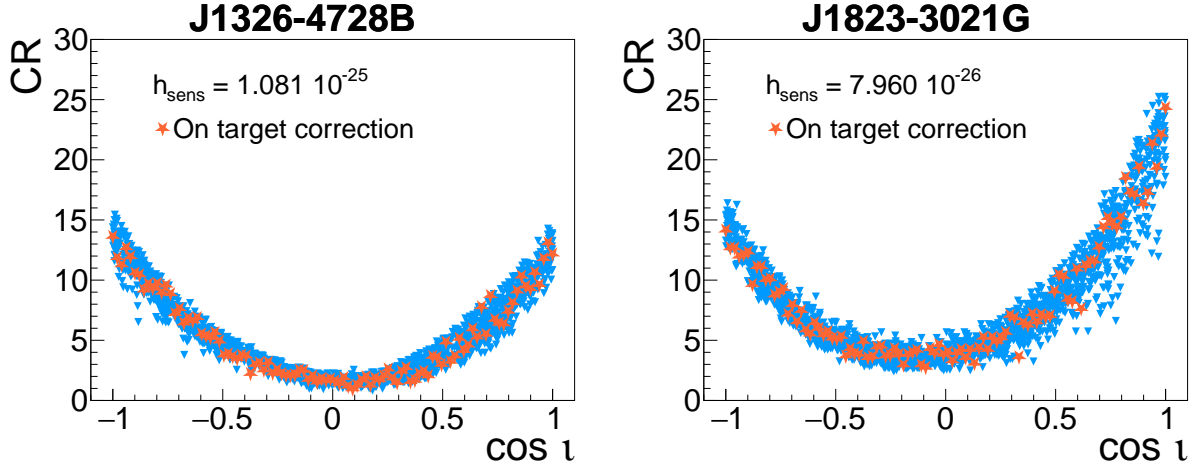


Figure 7. Same as in Fig.3 but with uncertainties on orbital parameters enlarged by an order of magnitude (i.e., the coherence time of the targets is reduced by the same factor, see Eq.(24)). The additional test, made to ensure the behaviour for $T_{FFT} < T_{sid}/5$ (see Sec.IV A), did not highlight any strong dependence on the offset in the orbital parameters as in Sec.IV C.

construction of Advanced LIGO and construction and operation of the GEO600 detector. Additional support for Advanced LIGO was provided by the Australian Research Council. Virgo is funded, through the European Gravitational Observatory (EGO), by the French Centre National de Recherche Scientifique (CNRS), the Italian Istituto Nazionale di Fisica Nucleare (INFN) and the Dutch Nikhef, with contributions by institutions from Belgium, Germany, Greece, Hungary, Ireland, Japan, Monaco, Poland, Portugal, Spain. KAGRA is supported by Ministry of Education, Culture, Sports, Science and Technology (MEXT), Japan

Society for the Promotion of Science (JSPS) in Japan; National Research Foundation (NRF) and Ministry of Science and ICT (MSIT) in Korea; Academia Sinica (AS) and National Science and Technology Council (NSTC) in Taiwan.

We would like to acknowledge CNAF for providing the computational resources.

We would like to also acknowledge the ATNF Pulsar Catalogue, R. N. Manchester, R. N. Manchester, G. B. Hobbs, A. Teoh & M. Hobbs, *Astronomical Journal*, 129, 1993-2006 (2005), see <http://www.atnf.csiro.au/research/pulsar/psrcat> for updated versions.

-
- [1] B. T. Reed, A. Deibel, and C. J. Horowitz, *The Astrophysical Journal* **921**, 89 (2021).
 - [2] H. Hakobyan et al., *Astrophys. J.* **943**, 105 (2023).
 - [3] B. J. Owen, *Phys. Rev. Lett.* **95**, 211101 (2005).
 - [4] B. Rajbhandari, B. J. Owen, S. Caride, and R. Inta, *Phys. Rev. D* **104**, 122008 (2021).
 - [5] O. J. Piccinni, *Galaxies* **10**, 72 (2022).
 - [6] B. P. Abbott et al. (LIGO Scientific Collaboration and Virgo Collaboration), *Phys. Rev. D* **96**, 062002 (2017).
 - [7] B. P. Abbott et al. (LIGO Scientific Collaboration and Virgo Collaboration), *Phys. Rev. D* **100**, 024004 (2019).
 - [8] R. Abbott et al. (LIGO Scientific Collaboration, Virgo Collaboration, and KAGRA Collaboration), *Phys. Rev. D* **106**, 102008 (2022).
 - [9] B. P. Abbott et al. (LIGO Scientific Collaboration and Virgo Collaboration), *Phys. Rev. D* **94**, 102002 (2016).
 - [10] E. Goetz and K. Riles, *Classical and Quantum Gravity* **28**, 215006 (2011).
 - [11] R. Abbott et al. (The LIGO Scientific Collaboration and the Virgo Collaboration), *Phys. Rev. D* **103**, 064017 (2021).
 - [12] P. B. Covas and A. M. Sintes, *Phys. Rev. Lett.* **124**, 191102 (2020).
 - [13] R. Abbott et al. (LIGO Scientific, VIRGO, KAGRA), *Astrophys. J.* **935**, 1 (2022).
 - [14] R. Abbott et al. (LIGO Scientific Collaboration, Virgo Collaboration, and KAGRA Collaboration), *Phys. Rev. D* **105**, 022002 (2022).
 - [15] P. Leaci et al., *Phys. Rev. D* **95**, 122001 (2017).
 - [16] J. T. Whelan et al., *The Astrophysical Journal* **949**, 117 (2023).
 - [17] R. Abbott et al., *The Astrophysical Journal Letters* **941**, L30 (2022).
 - [18] L. D’Onofrio et al., *Phys. Rev. D* **108**, 122002 (2023).

- [19] A. Singhal et al., *Classical and Quantum Gravity* **36**, 205015 (2019).
- [20] B. P. Abbott et al. (LIGO Scientific Collaboration and Virgo Collaboration), *Phys. Rev. D* **96**, 122006 (2017).
- [21] B. P. Abbott et al. (LIGO Scientific Collaboration and Virgo Collaboration), *Phys. Rev. Lett.* **120**, 031104 (2018).
- [22] R. Abbott et al. (LIGO Scientific Collaboration, Virgo Collaboration, and KAGRA Collaboration), *Phys. Rev. D* **106**, 042003 (2022).
- [23] B. P. Abbott et al. (LIGO Scientific Collaboration and Virgo Collaboration), *Phys. Rev. D* **95**, 082005 (2017).
- [24] P. Leaci and R. Prix, *Phys. Rev. D* **91**, 102003 (2015).
- [25] M. Tse et al., *Phys. Rev. Lett.* **123**, 231107 (2019).
- [26] F. Acernese et al. (Virgo Collaboration), *Phys. Rev. Lett.* **123**, 231108 (2019).
- [27] P. Jaranowski and A. Królak, *Phys. Rev. D* **61**, 062001 (2000).
- [28] J. Abadie et al., *The Astrophysical Journal* **737**, 93 (2011).
- [29] G. B. Hobbs, R. T. Edwards, and R. N. Manchester, *Monthly Notices of the Royal Astronomical Society* **369**, 655 (2006), ISSN 0035-8711.
- [30] R. T. Edwards, G. B. Hobbs, and R. N. Manchester, *Monthly Notices of the Royal Astronomical Society* **372**, 1549 (2006), ISSN 0035-8711.
- [31] R. N. Manchester, G. B. Hobbs, A. Teoh, and M. Hobbs, *The Astronomical Journal* **129**, 1993 (2005).
- [32] C. C. Miao et al., *Monthly Notices of the Royal Astronomical Society* **518**, 1672 (2022), ISSN 0035-8711.
- [33] M. Cruces et al., *Monthly Notices of the Royal Astronomical Society* **508**, 300 (2021), ISSN 0035-8711.
- [34] P. Astone et al., *Phys. Rev. D* **90**, 042002 (2014).
- [35] O. J. Piccinni et al., *Class. Quant. Grav.* **36**, 015008 (2019).
- [36] P. Astone, S. Frasca, and C. Palomba, *Classical and Quantum Gravity* **22**, S1197 (2005).
- [37] S. D’Antonio et al., *Phys. Rev. D* **108**, 122001 (2023).
- [38] R. Abbott et al. (KAGRA, VIRGO, LIGO Scientific), *Astrophys. J. Suppl.* **267**, 29 (2023).
- [39] R. Abbott et al., *The Astrophysical Journal Supplement Series* **267**, 29 (2023).
- [40] B. P. Abbott et al., *The Astrophysical Journal* **882**, 73 (2019).
- [41] P. Jaranowski, A. Królak, and B. F. Schutz, *Phys. Rev. D* **58**, 063001 (1998).